Finite element–based assessment of energy harvesting in composite beams with piezoelectric transducers

Article *in* Proceedings of the Institution of Mechanical Engineers Part L Journal of Materials Design and Applications · October 2021

DOI: 10.1177/14644207211046585

CITATIONS
3

READS
242

6 authors, including:

Theofanis Plagianakos
Hellenic Aerospace Industry
35 PUBLICATIONS **534** CITATIONS
SEE PROFILE

Nikolaos Margelis
National Technical University of Athens
7 PUBLICATIONS **9** CITATIONS
SEE PROFILE

Nikolaos Leventakis
National and Kapodistrian University of Athens
14 PUBLICATIONS **32** CITATIONS
SEE PROFILE

Georgios Bolanakis
National Technical University of Athens
7 PUBLICATIONS **13** CITATIONS
SEE PROFILE

Original article

Institution of MECHANICAL ENGINEERS
Journal of MATERIALS: DESIGN AND APPLICATIONS

Proc IMechE Part L:
J Materials: Design and Applications
1–16

DOI: 10.1177/14644207211046585
journals.sagepub.com/home/pil
SAGE

Finite element-based assessment of energy harvesting in composite beams with piezoelectric transducers

Theofanis S. Plagianakos[1], Nikolaos Margelis[1], Nikolaos Leventakis[1], Georgios Bolanakis[1], Panagiotis Vartholomeos[2] and Evangelos G. Papadopoulos[1]

Abstract

A finite element-based methodology is introduced for studying composite beams with piezoelectric transducers connected to energy harvesting circuits. Continuous and lumped-parameter models are developed based on finite element approximations and verified by means of experiments performed on a cantilever beam subjected to sinusoidal excitation at low, with respect to resonance, frequencies below 15 Hz. Three harvesting circuits have been studied: an in-house, a commercial, modified to include a rectification stage, and an off-the-shelf commercial. Comparison of numerical predictions with experiments illustrates good agreement in voltage and high sensitivity to current losses in the circuit. It was found that the commercial circuits outperform the in-house circuit in terms of harvested power at frequencies higher than 5 Hz, while the latter enables power harvesting at arbitrary low frequencies. Based on these results, it is demonstrated that the developed approach enables coupled simulation of a composite structure and a realistic harvesting circuit in one-shot.

Keywords

Piezoelectric, energy harvesting, composite beam, finite element, multiphysics simulation, commercial harvesting circuits

Date received: 28 April 2021; accepted: 30 August 2021

Introduction

Piezoelectric Energy Harvesting (PEH) refers to the two-stage process of (i) mechanical to electric energy conversion via a piezoelectric (PE) transducer during structural vibration and (ii) energy storage by means of an appropriately designed electric circuit. Pioneering autonomous systems including PE sensors and suitable harvesting circuits have been designed quite early.[1,2] In the last two decades, PEH has become an emerging research field, mainly due to its high efficiency compared to other physical mechanisms.[3] Its main applications include exploitation of the energy produced by human motion or ambient vibration by providing low power to electronic equipment in the context of IoT solutions.[4–6]

A vibrating PE element, responsible for the first PEH stage, behaves electrically as a capacitive AC source, which must be rectified at a desired DC voltage level to be useful for powering an electronic device or energy storage element. The simplest configuration of PEH, that realizes both stages, comprises the PE element, an AC-DC diode rectifier and a switched-mode DC-DC converter to provide the DC power to the load.[7] Adaptive circuits have been designed for maximizing the power transfer,[8,9] whereas nonlinear techniques employing capacitor-inductor resonant circuits (SSHI)[10,11] tend to increase the harvested energy. The virtues of SSHI were combined with adaptive power transfer, resulting in SSHI circuits operated by a maximum power point tracking algorithm (MPPT).[12] A bias-flip rectifier that can improve upon the power extraction capability of existing full-bridge rectifiers by more than 4 times was presented in.[13] Most of the systems mentioned above employ linear PE oscillators, which are exclusively studied near their resonant frequencies. On the other hand, non-linear PE harvesters may be tuned to increase the frequency range, the power amplitude, and the responsiveness to non-sinusoidal noisy excitations.[14–16]

PEH mechanisms have been modeled mainly as lumped-parameter systems[17–23] due to low computational

[1]Control Systems Lab - School of Mechanical Engineering, National Technical University of Athens, Athens, Greece.
[2]University of Thessaly, Department of Computer Science and Biomedical Informatics.

Corresponding author:
Theofanis S. Plagianakos, Mechanical Engineer PhD
Email: fanplag@gmail.com

cost and compatibility with the electric circuit model. However, the fatigue performance of the coupled electromechanical system depends on local effects, such as stress distribution in the mechanical subcomponents, which can be captured exclusively by modeling the continuum solid. Solutions based on Hamilton's principle, such as Ritz-type and finite element (FE) methodologies, are candidate approaches. A Ritz-type solution has been formulated by Jacquelin et al.[24] for simulating the impact response of a PE unimorph connected to a resistive circuit. Benasciutti et al.[25] used FE modeling for optimizing the strain distribution along a PE unimorph by implementing a curved supporting block. Optimization of the dissipated power in terms of damping and electromechanical coupling in a resistively shunted unimorph has been performed.[26] A micro-energy harvester operating below 100 Hz excitation has been developed.[27] Niasar et al.[28] studied the power output design of a roadway PEH in terms of geometric parameters and material properties by using FE models for resistive circuits and implemented Simulink for predicting power output in SSHI and SEH circuits. They also extended their approach for studying electrical fatigue of PEH and implemented relevant design optimization.[29] Recently, FE models for resistively shunted piezoelectric devices in geometric nonlinear regime have been reported.[30,31] Most of the above-mentioned FE models are capable of predicting the vibration response of resistively shunted electromechanical systems. Moreover, the excitation is typically near resonance.

The present work aims at developing a FE based methodology for supporting structural design of composite beams with PEH circuits. The purpose of the study is mainly to validate the models developed and compare the selected harvesting circuits at a low-frequency range, off-resonance. The developed FE models are shown to predict the electromechanical response of the composite structure coupled to the harvesting circuit in one shot. Three FE types are studied, illustrating their accuracy and computational efficiency. A lumped-parameter alternative to the one-shot approach is also developed. To validate the methodology, three harvesting circuits are experimentally studied: an in-house, a commercial, modified to include a rectification stage, and an off-the-shelf commercial. Results show the validity of the developed methodology, and its possible usage to further study coupled systems.

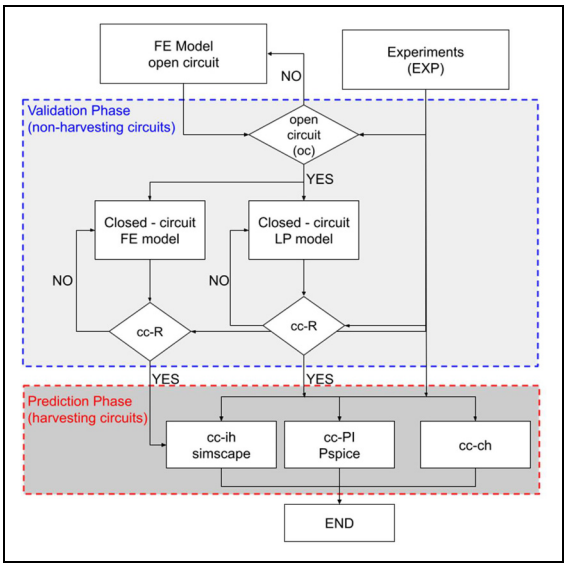

Figure 1. Overview of the modeling approach.

Electromechanical system model

The electromechanical system studied is a cantilever composite beam with a shunted PE patch subjected to forced harmonic excitation. In the validation phase, which includes open-circuit (oc) and resistive circuit (cc-R) configurations, the matrices derived from in-house and commercial FE codes are fed as stiffness, mass, damping, and piezoelectric, dielectric constants into lumped-parameter models.

In the prediction phase three PEH circuits are studied: an in-house circuit (cc-ih) of known parameters, and two commercial circuits of unknown architecture and parameters. One of the latter (cc-PI) is reversed-engineered, while the other (cc-ch) is modified to include a rectification stage and is used for harvested power comparison. The modeling approach flowchart is schematically shown in Figure 1. In the next sections each model is described explicitly.

PEH FE model

The beam geometry is shown in Figure 2 and the relevant geometric parameters are listed in Table 1. The PE patch is bonded with epoxy on the upper surface of the beam and is assumed to be tightly connected with the beam.

The PE material is polarized along its thickness; in the context of this work, it exhibits linear PE behavior. The ply constitutive equations in the natural coordinate system Oxyz have the form

$$\begin{aligned} \sigma_i &= C_{ij}^{E} S_j - (e_{3i})^T E_3 \\ D_3 &= e_{3j} S_j + \epsilon_{33}^{S} E_3 \end{aligned} \tag{1}$$

where $i, j = 1,\ldots,6$; σ_i and S_j are the mechanical stress and engineering strain in vectorial notation; E_3 is the component of electric field vector along the thickness direction; D_3 is the electric displacement vector component; C_{ij} is the elastic stiffness tensor; e_{3j} is the piezoelectric tensor arising from the piezoelectric charge tensor and the stiffness tensor; and ϵ_{33} is the material electric permittivity. Superscripts E and S indicate constant electric field and strain conditions, respectively, and T indicates matrix transposition. Equation (1) is valid for an arbitrary laminate material, as it covers the behavior of both the PE and passive composite plies ($e_{mj} = 0$). The indices in Equation (1) denote that the present continuum models account for the full representation of the stress and strain tensors in 3D space and may be applied to arbitrary

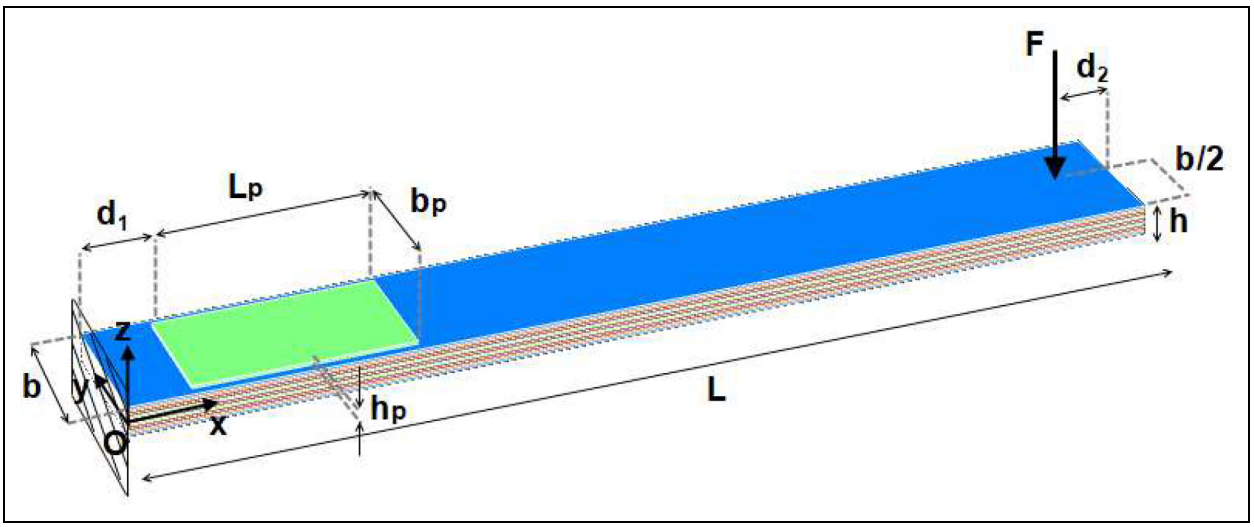

Figure 2. Composite beam with piezoelectric (PE) patch.

geometries, laminations, and sensor configurations.

The electric field vector component E_3 is the gradient of the electric potential υ along the thickness of the PE patch:

$$E_3 = -\partial \upsilon / \partial z \tag{2}$$

Three FE models were developed in the multiphysics commercial software Comsol[32]: (i) a 3-D solid element model (3D-sFE), (ii) a 2-D plane strain model (2D-psFE) and (iii) a layerwise shell element model (2D-lsFE). Without loss of generality the formulation is derived for the layerwise shell case (Figure 3). Typical through-thickness kinematic assumptions of the linear layerwise theory[33] are expressed as:

$$\begin{aligned} u^k(x,y,\zeta_k) &= U^k(x,y)\Psi_1^k(\zeta_k) + U^{k+1}(x,y)\Psi_2^k(\zeta_k) \\ v^k(x,y,\zeta_k) &= V^k(x,y)\Psi_1^k(\zeta_k) + V^{k+1}(x,y)\Psi_2^k(\zeta_k) \\ w^k(x,y,\zeta_k) &= W^k(x,y)\Psi_1^k(\zeta_k) + W^{k+1}(x,y)\Psi_2^k(\zeta_k) \\ \upsilon^k(x,y,\zeta_k) &= Y^k(x,y)\Psi_1^k(\zeta_k) + Y^{k+1}(x,y)\Psi_2^k(\zeta_k) \end{aligned} \tag{3}$$

where index k denotes the discrete layer, u, v, and w, are the displacements along x, y, and z, respectively, and υ is the electric potential. U, V, W and Y are the respective variable values at the interfaces between discrete layers, practically denoting degrees of freedom of the piezocomposite laminate. The kinematic assumptions of Equation (3) account for any type of composite layer and active or sensory PE layer, such as piezoceramic, piezopolymer, encapsulated piezoelectric and macro-fiber, the latter with unit-cell layer properties. In this work each material and PE sensor/actuator is modeled in a separate layer and piezoceramic layers polarized along the z-axis are modeled and used in the tests. The linear layerwise displacement-potential approach rests on linear functions of discrete layer thickness in a local coordinate system ($\zeta_k \in [-1,1]$), given by

$$\begin{aligned} \Psi_1^k &= (1-\zeta_k)/2 \\ \Psi_2^k &= (1+\zeta_k)/2 \end{aligned} \tag{4}$$

The governing equations of motion are provided in energy terms form as,

$$\begin{aligned} &\int_{t_0}^{t_0+\mathrm{d}t} \left(\int_{A_0} \delta K_L \,\mathrm{d}x\,\mathrm{d}y - \int_{A_0} \delta H_L \,\mathrm{d}x\,\mathrm{d}y \right. \\ &\left. - \int_{A_0} \delta W_{\mathrm{d}L} \,\mathrm{d}x\,\mathrm{d}y + \int_{\Gamma} \delta \bar{u}^T \bar{\tau} \,\mathrm{d}\Gamma \right) \mathrm{d}t = 0 \end{aligned} \tag{5}$$

where subscript L denotes composite laminate, A_0 is the midplane, $\delta\bar{u}$ is the vector of all mechanical degrees of freedom of the laminate arising from the kinematic assumptions in Equation (3), $\bar{\tau}$ are the tractions at the boundary surface Γ and $\delta \mathrm{H}_L$, δK_L and δW_{d_L} are the variations of the electromechanical, kinetic and dissipated energy of the laminate per unit area, respectively.

Incorporation of Equations (1)–(4) in (5), in-plane approximation of mechanical and electric variables using quadratic Serendipity shape functions and integration along mid-surface yields the discretized system matrices. Characteristic mesh types and densities applied to the current models are shown in Figure 4.

Table 1. Beam and PE element geometric parameters.

Parameter	Value (mm)	Parameter	Value (mm)
beam length L	233	PE patch length L_p	50
beam width b	35	PE patch width b_p	30
… beam thickness h	2.15	PE patch thickness h_p	0.2
distance from support, d_1	15	distance from free end, d_2	18

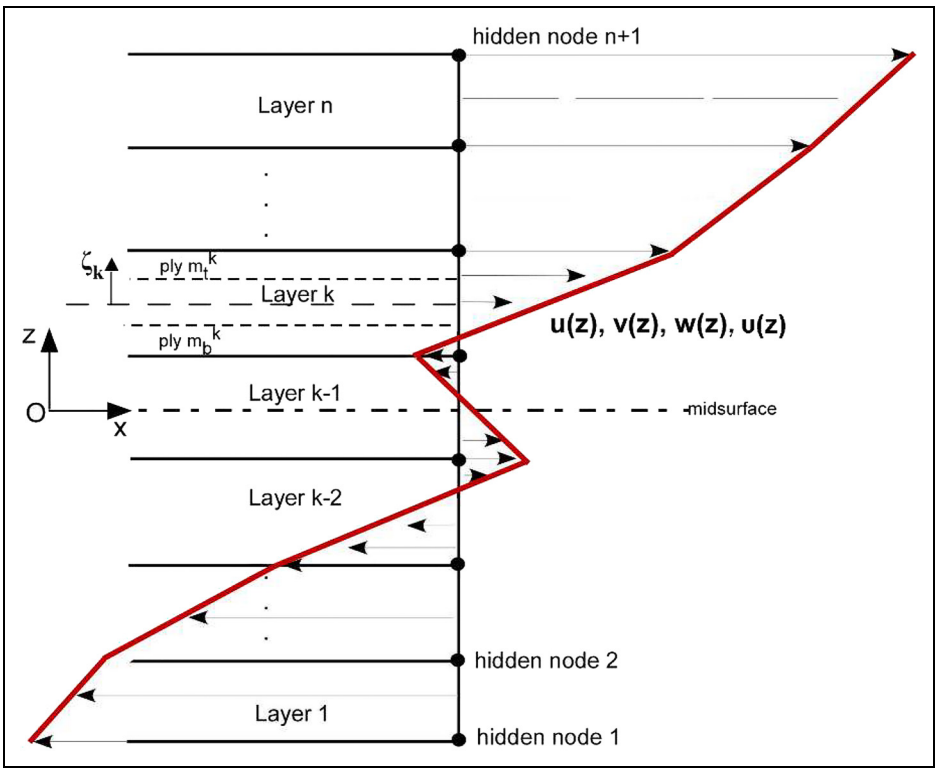

Figure 3. General form of through-thickness distribution of displacements and electric potential.

It should be noted that the formulations of the 3D-sFE and 2D-psFE[32] do not allow for orthotropic composite ply properties and stacking sequence input. Thus, equivalent single-ply properties are derived based on ply compliance transformation to natural coordinate system Oxyz (Figure 2) and averaging for the balanced symmetric composite laminate under consideration.[34]

In the case of a circuit connected to the PE terminals, as in the typical case of a resistive load, the response of the discretized system is described by,[35]

$$\begin{bmatrix} [M_{uu}] & 0 \\ 0 & 0 \end{bmatrix} \begin{Bmatrix} \ddot{\bar{u}} \\ \ddot{v} \end{Bmatrix} + \begin{bmatrix} [C_{uu}] & 0 \\ 0 & 0 \end{bmatrix} \begin{Bmatrix} \dot{\bar{u}} \\ \dot{v} \end{Bmatrix} + \begin{bmatrix} [K_{uu}] & [K_{uv}] \\ [K_{vu}] & [K_{vv}] \end{bmatrix} \begin{Bmatrix} \bar{u} \\ v \end{Bmatrix} = \begin{Bmatrix} F(t) \\ Q(t) \end{Bmatrix} \tag{6}$$

$$C_p\{\dot{v}\} + \frac{1}{R}\{v\} = \{\dot{Q}(t)\} = \{I(t)\} \tag{7}$$

where $[M]$, $[C]$ and $[K]$ are the system mass, damping and stiffness matrices, C_p is the capacity of the PE patch, F is the applied force vector and Q and I are, respectively, the electric charge and current in the circuit. Note that the damping considered in Equation (6) is exclusively attributed to the viscoelastic nature of the composite material and the friction in the supports. Based on measurements and engineering practice, this damping is low, thus not affecting the system eigenfrequencies.

The system of Equations (6) and (7) describes the forced harmonic response in the case of a shunted resistance. In the case of a more complicated load than the one in Equation (7), this equation can be formulated using the load impedance. In the general case of an arbitrary harvesting circuit, this can be addressed by exploiting commercial software capabilities. Thus, the present continuum model provides a solution for the electromechanical system coupled with the PEH circuit in one shot. Alternatively, to implement complex circuits efficiently in terms of computational effort, the continuum model may be used for providing input to the lumped parameter model presented in the next section.

The harvested power from the PEH circuit may be calculated using the energy stored in the output of the discharging subcircuit between two timestamps as,

$$P(t) = \frac{\int_{t_1}^{t_2} v(t)I(t)\,\mathrm{d}t}{t_2 - t_1} \tag{8}$$

Lumped-parameter model of electromechanical system with harvesting circuit

The general formulation of the LP model implemented herein has been developed by Erturk and Inman.[3] Combining the analytical bending solution with a resistive circuit element equation provides the circuit current source as,

$$I(t) = -\sum_{j=1}^{\infty} \kappa_j \frac{\mathrm{d}\eta_j(t)}{\mathrm{d}t} \tag{9}$$

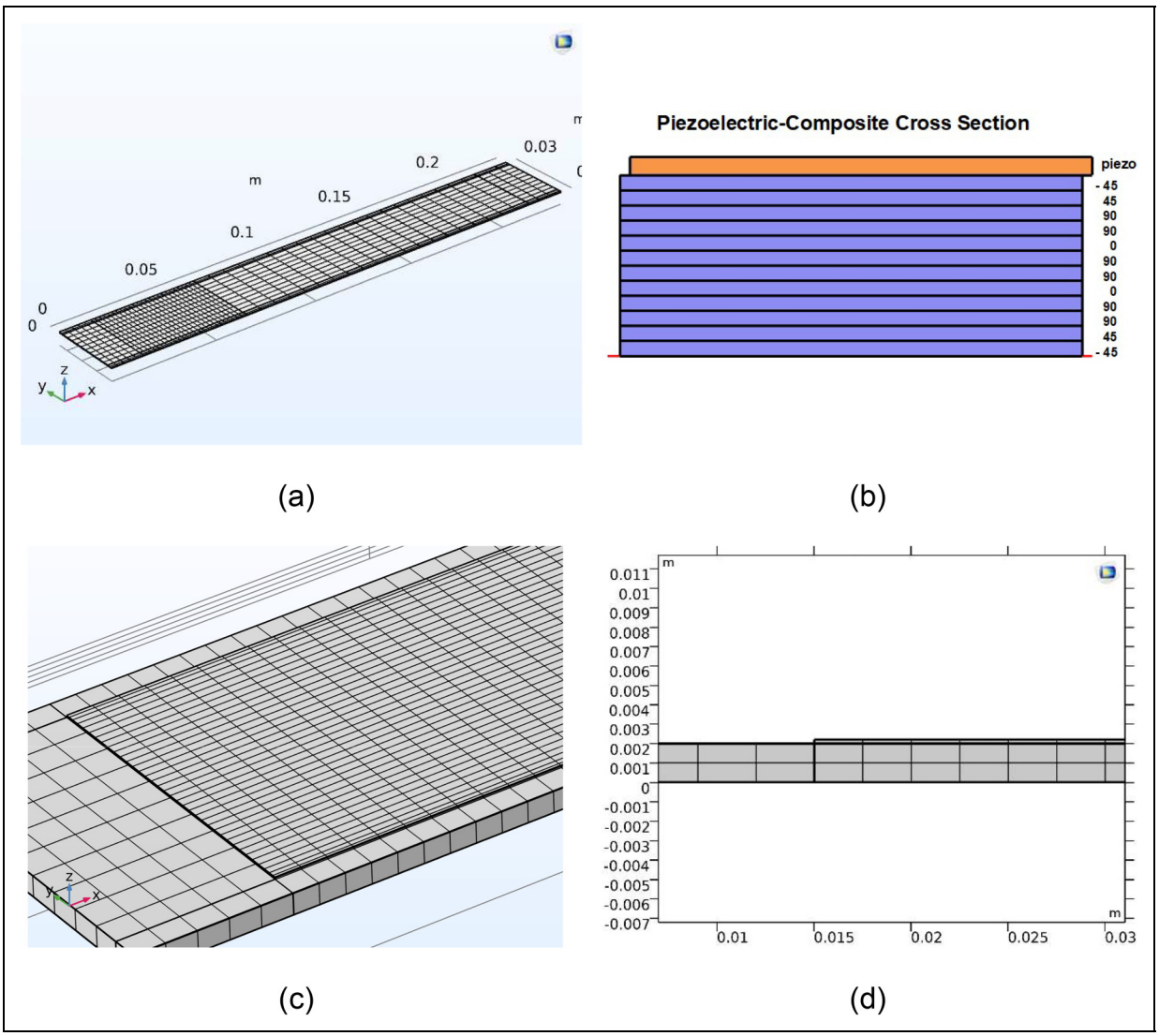

Figure 4. Finite element meshes considered: (a)-(b): 2D-lsFE with through-thickness discretization, (c) 3D-sFE, (d) 2D-psFE.

where j denotes an eigenmode, η is the transient vector of modal coordinates in the space-time decomposition of the transverse displacement,

$$w(x,\,t) = \sum_{j=1}^{\infty} \varphi_j(x)\eta_j(t) \tag{10}$$

where φ denotes the eigenvector of mode j and κ is the modal electromechanical coupling coefficient,

$$\begin{aligned}\kappa_j &= e_{31}h_p b\int_{x_s}^{x_f}\frac{\mathrm{d}^2\varphi_j(x)}{\mathrm{d}x^2}\,\mathrm{d}x \\ &= e_{31}h_p b\left(\left.\frac{\mathrm{d}\varphi_j(x)}{\mathrm{d}x}\right|_{x_f} - \left.\frac{\mathrm{d}\varphi_j(x)}{\mathrm{d}x}\right|_{x_s}\right)\end{aligned} \tag{11}$$

with x_s and x_f denoting start and end of the patch in terms of the length coordinate x.

The methodology followed for determining stiffness, mass, damping, piezoelectric and permittivity terms of the LP model, including all necessary terms appearing in Equations (9)–(11) may be briefly summarized as:

(a) Solving of Equation (6) for the free-vibration response of the open-circuit system in the frequency domain provides the eigenvectors, which are used for the formulation of the modal mass, damping, stiffness, and force transformation matrices, respectively[36]:

$$\begin{aligned}[M_{ff\,\mathrm{mod}}] &= [\varphi]^{\mathrm{T}}[M][\varphi] \\ [C_{ff\,\mathrm{mod}}] &= [\varphi]^{\mathrm{T}}[C][\varphi] \\ [K_{ff\,\mathrm{mod}}] &= [\varphi]^{\mathrm{T}}[K][\varphi] \\ [F_{sf\,\mathrm{mod}}] &= [\varphi]^{\mathrm{T}}[F]\end{aligned} \tag{12}$$

(b) The modal matrices are used for determining η:

$$\begin{aligned}&[M_{ff\,\mathrm{mod}}]\{\ddot{\eta}\} + [C_{ff\,\mathrm{mod}}]\{\dot{\eta}\} + [K_{ff\,\mathrm{mod}}]\{\eta\} \\ &\quad = \{F_{sf\,\mathrm{mod}}\}\end{aligned} \tag{13}$$

(c) The electromechanical coupling coefficient κ is provided by Equation (11) using PE properties, geometrical parameters, and the slope of the modal transverse displacement. The latter is directly calculated in modal space, in addition to eigenvectors and modal matrices, by implementing a C^1-continuous 2D higher-order layerwise FE,[37] which encompasses this slope as a nodal DOF.
(d) The electric current flowing through the PEH circuit is calculated using Equation (9). As an alternative to points (b)–(c), η may be measured at the point of excitation by means of a high-speed camera.
(e) The PE transducer is modeled in the PEH circuit as a current source and a capacitor with C_p appearing in Equation (7) and derived as:

$$C_p = \frac{\varepsilon_{33} b L}{h_p} \tag{14}$$

The LP model is implemented in Simscape[38] and PSpice[39] software.

PEH circuits

As mentioned earlier, the PEH circuits studied were the in house (cc-ih), the custom using off-the-shelf commercial hardware (cc-ch)[40] and the commercial, designated as the E-821.00 electronic module by PI (cc-PI).[41] In general, their architectures follow established designs[7] including three main parts, i.e. a rectifier, a charging capacitor, and a discharging switch (MOSFET).

In-house PEH circuit (cc-ih)

The in-house circuit (Figure 5) consists of a diode rectifier due to the alternating input current, a capacitor which is charged by the rectified electric current and a load with a MOSFET switch which discharges the capacitor.

The in-house circuit is designed as simple as possible because its main purposes are model validation and design exploration. As shown in Figure 5, the circuit consists of a diode rectifier – due to alternating current from the oscillating PE transducer – in parallel with a capacitor which accumulates charge. The current provided by the PE transducer component is independent of the electric circuit. A MOSFET acts as a load switch. When it does not conduct, the capacitor is charged, else it is discharged providing current to the resistive load. Selecting properly the capacitor capacitance and upper and lower voltage thresholds, different types of loads including batteries can be powered.

Custom commercial circuit (cc-ch)

The custom commercial harvesting circuit has been developed for comparison in terms of harvested power. It is based on the SPV1050, an ultralow power, high-efficiency energy harvester and battery charger manufactured by STMicroelectronics.[40] The SPV1050 is an Integrated Circuit (IC) that implements the maximum power point tracking function (MPPT) and incorporates the switching elements of a buck-boost converter. However, it lacks the rectifying stage needed for piezoelectric sources, as it is intended for photovoltaic applications. To this end, a full-wave rectifier has been designed and implemented in-house (Figure 6(a),b). The rectifier includes a Zener diode to protect the energy harvester against voltage overshoots.

A schematic representation of the custom commercial harvesting circuit is shown in Figure 6(c). The piezoelectric element is connected to the full-wave rectifier, the output of which is provided directly to the STEVAL-ISV020V1, an evaluation board provided by STM icroelectronics that integrates the SPV1050 and its purpose is to facilitate the development of applications based on it. A single-cell LiPo battery is connected to the evaluation board's output. Throughout the experiments described in the next section, the low-dropout regulators have been disabled, leaving the battery charging and MPPT functions enabled.

Commercial circuit (cc-PI)

The commercial circuit E-821.00 manufactured by PI,[40] shown in Figure 7(a) is an integrated circuit that includes a diode rectifier and a capacitor that charges due to the alternative current produced by the PE transducer. Reverse engineering of the circuit may lead to the PSpice[39] model presented in Figure 7(b).

When the voltage of the capacitor reaches a reference value of 12 V, an automatic switch is activated, allowing part of the electric energy in the capacitor to be released into a secondary sub-circuit. The automatic switch is turned off when the voltage of the capacitor falls at 6 V. The switch is implemented by a MOSFET controlled by an operational amplifier which compares the voltage of the capacitor to the reference voltage. This response is modeled with the use of a Schmitt trigger supplied by external voltage sources for simplicity. The secondary circuit consists of a buck converter that assures that the output of E-821.00 is a pulse of constant voltage. In the model presented in Figure 7(b), the function of the secondary circuit is modeled by a simplified buck converter and a voltage clipper to reduce the complexity of the model. The simplified version of the buck converter includes a feedback loop, so that the harvesting circuit output to a resistor is a pulse of constant voltage. The feedback loop is implemented with two operational amplifiers and a MOSFET. Like the Schmitt trigger sub-circuit, parts of the feedback loop are connected to external voltage sources, whereas the buck converter of the actual circuit is supplied partly by the electric energy produced by the PE transducer.

Experimental configuration

An experimental setup was developed to facilitate the acquisition of measurements, see Figure 8. The harvested

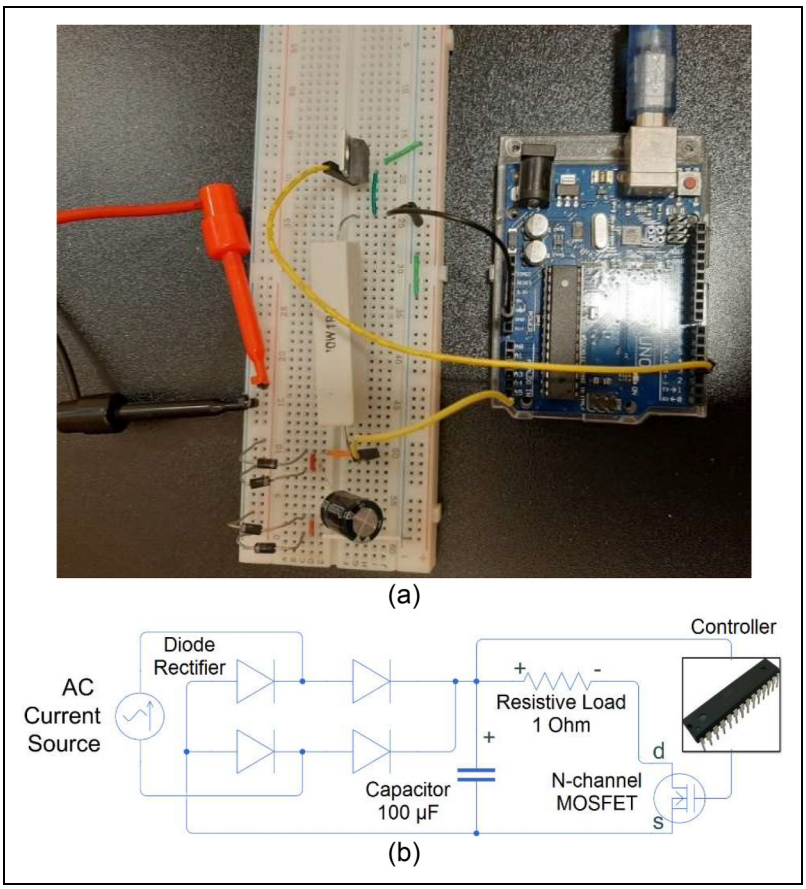

Figure 5. In-house harvesting circuit (cc-ih): (a) physical representation, (b) systems modeling approach.

energy was provided by a P.876-A12 DuraAct® patch from PI,[42] glued with epoxy on the beam upper surface. An LDS V201 (B&K) shaker was used to excite the specimen through a steel stinger instrumented with a load cell (PCB). Additional signals were acquired by an accelerometer (PCB) and a fine current sensor with adjustable range (nA, μA or mA). All signals were collected by a NI 2110 BNC-terminal block and a NI PCI-6036E DAQ board. Labview® software was used for providing the excitation signal to be amplified by an LDS LPA100 B&K amplifier, as well as, for measurement storage. The displacement at the load application point was measured by processing images[43] acquired by a high-speed camera.

Comparison of measurements with model predictions revealed that using the measured force as model input yields higher displacement amplitudes than measured. This is attributed to the stinger's free length and inertia effects of the concentrated mass of the load cell, indicating deviation from a "rigid" exciter of zero mass. Moreover, the shaker is voltage-controlled, setting mechanical displacements at the load application point. Thus, the excitation input to the FE and LP models was provided in terms of displacement, as explicitly reported in Section 5.

The electrical response of the PEH circuits is studied by measuring voltage and current both at the terminals of the PE element and at the output of each circuit. Voltage was measured using a DAQ board analog channel, while current by a Low Power Lab sensor, exhibiting accuracy of ±0.05% for both the μA and nA ranges.

Results and discussion

The models developed are validated against measurements for resistive and harvesting circuits. In addition, quantification of the alternative PEH circuits is studied in terms of power generation at a low frequency excitation regime, compared to system resonance.

Material properties

A composite beam of Graphite/Epoxy material with a surface attached piezoelectric patch and lamination $[-45/45/90_2/0/90]_S$ is studied. The elastic properties of the composite material considered are obtained from static tests[44] conducted by the manufacturer (Hellenic Aerospace Industry S.A.). They are additionally validat ed by performing modal tests on the beam leading to measurement of the fundamental eigenfrequency at 24.9 Hz. To yield measured damping in the fundamental bending mode ($\zeta = 2.4\%$), the composite ply damping coefficients have been fitted as to include damping due to friction in the clamped support. The electromechanical properties of beam and patch materials are listed in Table 2.

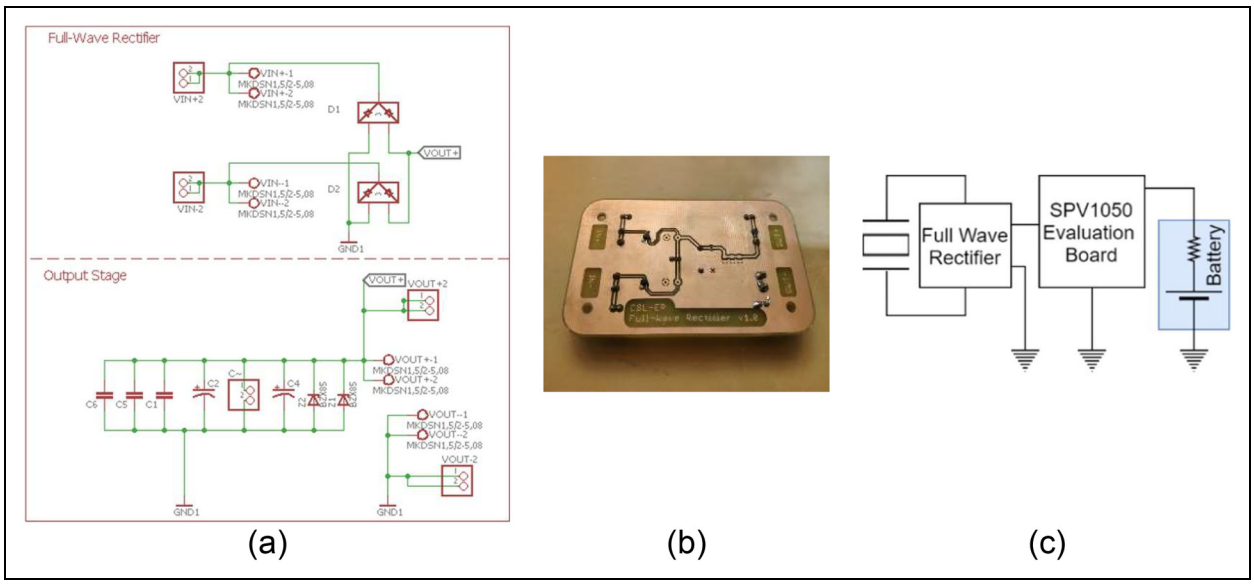

Figure 6. Custom commercial harvesting circuit (cc-ch): (a) schematic diagram of the full-wave rectifier, (b) physical representation of the full-wave rectifier, (c) schematic representation of the harvesting circuit.

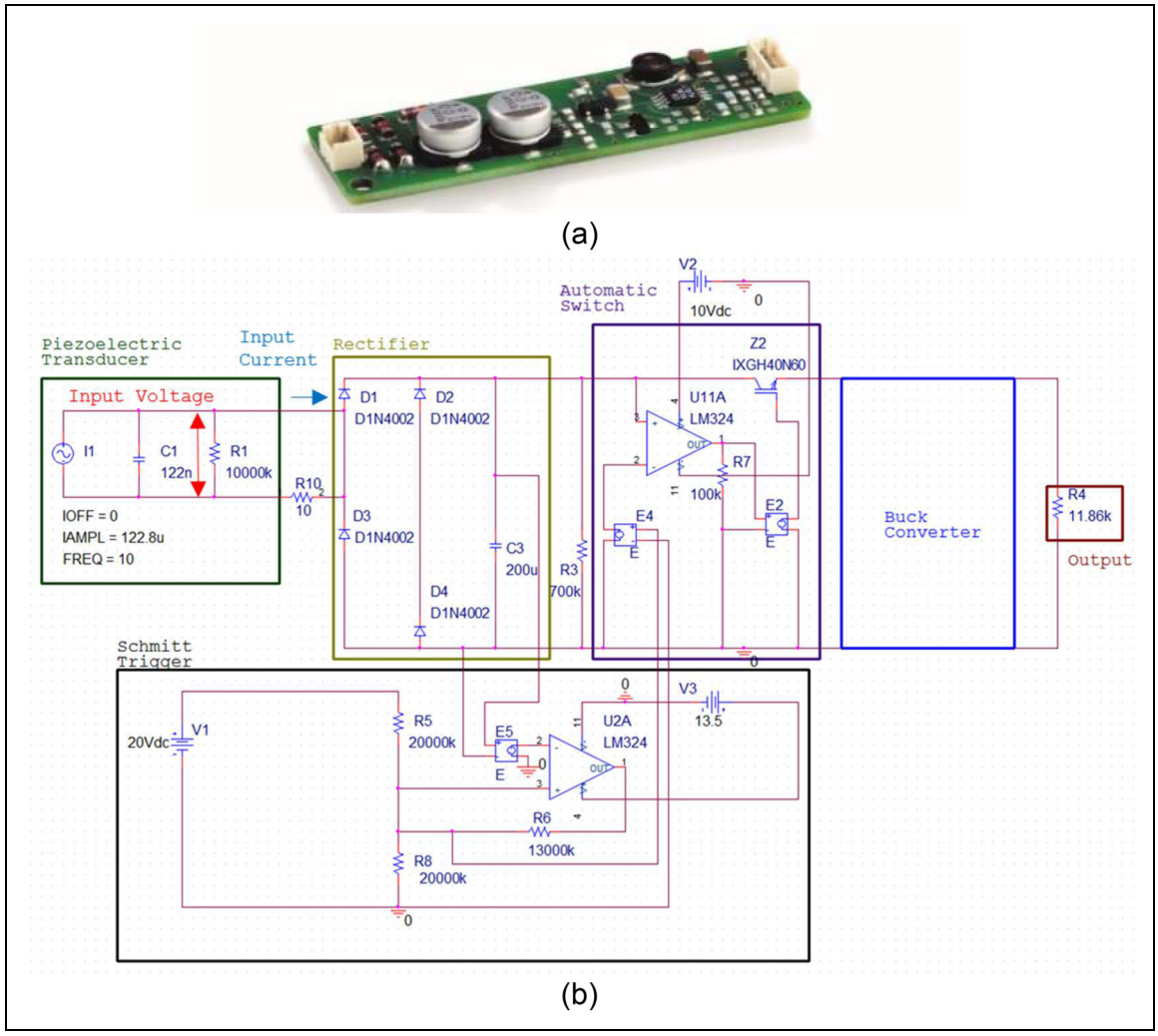

Figure 7. Commercial harvesting circuit (cc-PI): (a) physical representation, (b) reversed-engineered model including rectifier, Schmitt-trigger, voltage-clipper and buck-converter.

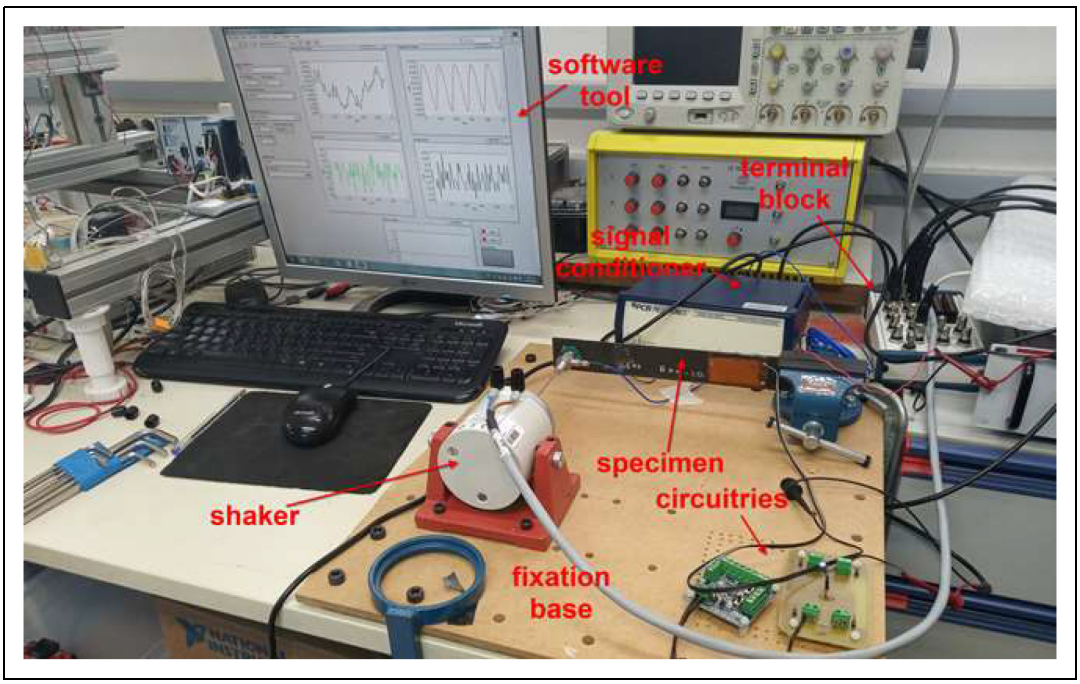

Figure 8. Experimental configuration.

Resistive-circuit (cc-R) response

The resistive circuit served as the simplest closed-circuit configuration to be studied in the context of model validation. An 11.8 kΩ resistor was connected at the terminals of the PE patch. Figure 9 shows predicted and measured values for the electric potential and current at the resistor terminals for a transverse displacement amplitude of $w_0 = 0.9$, 1.2 and 2.4 mm at 1, 10 and 20 Hz, respectively. This displacement was achieved with a force amplitude of $F_0 = 0.75$ N.

Some timesteps are required for the stabilization of the solution in the case of the FE models, reaching approximately half wave. In general, very good correlation is observed between predictions of 2D-lsFE and LP models and measurements for all frequencies studied. The 3D-sFE and 2D-psFE models overpredict both current and voltage. This deviation may be attributed to the approximation of the lamination as an equivalent UD-ply and the high thickness aspect ratio ($L/h = 108$) of the beam.

The measured response reveals a deviation from a pure sinusoidal response in the rising part of the sine wave and indicates a compulsion at the force application point. This compulsion may be attributed to the adjustment of the stinger on the specimen and the deflection caused by the concentrated mass of the load cell to the stinger.

Table 2. Electromechanical properties of materials considered (*: under constant stress).

Property	Composite Material	Piezoelectric Material
Density (kg/m^3)	1554	7800
Elastic Properties		
E_{11} (GPa)	138.40	62.10
E_{22} (GPa)	8.50	62.10
E_{33} (GPa)	8.50	48.30
G_{12} (GPa)	4.30	23.20
G_{13} (GPa)	4.30	21.30
G_{23} (GPa)	4.30	21.30
ν_{12}	0.31	0.33
ν_{13}	0.31	0.43
ν_{23}	0.31	0.43
Damping Properties		
ζ_{11} (%)	2.20	–
ζ_{22} (%)	19.20	–
ζ_{12} (%)	32.20	–
Piezoelectric Properties		
d_{31} (10^{-12} m/V)	–	−191
d_{32} (10^{-12} m/V)	–	−191
d_{33} (10^{-12} m/V)	–	409
Dielectric Properties ($\epsilon^0 = 8.85\ 10^{-12}$ F/m)		
ϵ_{33}/ϵ^0	3.5	1832*

PEH circuits response

In-house harvesting circuit (cc-ih). The voltage threshold for initiation of charging the capacitor by means of current produced by the PE transducer was set to 2.4 V. Figure 10 shows predicted and measured response in the charging sub-circuit at excitation frequency of 10 Hz.

It is observed that the LP model fairly predicts the measured amplitude of voltage and current, while there is some discrepancy in the timestamp of discharging initiation. Similar predictions are provided by the 2D-lsFE, although at a much higher computational cost. The discrepancy may be attributed to the deviation from

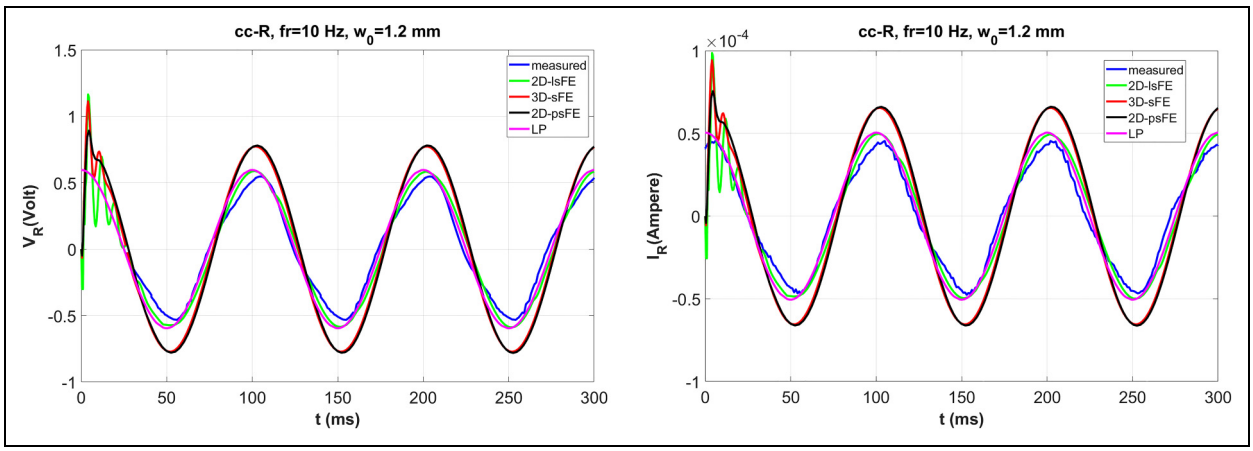

Figure 9. Resistive circuit: measured and predicted response at excitation frequency of 10 Hz.

sinusoidal excitation at the test, which does not occur in the models. Slight differences between nominal and actual electronic components' values also contribute to a relatively higher charging rate in the model compared to the experimental circuit. The spike in the predicted current of the LP model indicates discharging of the capacitor, which can be captured using an adaptive timestep during solution, effectively reaching the ns range. Overall, it was found that the response of the coupled electromechanical system with PEH is very sensitive to deviations in elastic and electric model parameters.

As also observed in Figure 10, the 2D-psFE model lacks in accuracy compared to the LP and 2D-lsFE FE model, as concluded also in the resistive circuit case, since it predicts higher eigenfrequencies and thus, stiffer response and shorter charging time. Nevertheless, it is more efficient compared to the 2D-lsFE shell in terms of computational cost. To this end, it may be used as a preliminary design tool for quick estimation of the induced mechanical stresses in the beam, which are critical for effective design against electromechanical fatigue of piezoelectric composite harvesters. The FE prediction of the coupled structure-circuit response in one-shot, as developed in this work, is thus a step towards improved design of harvesters.

Measured and predicted response in the output of the PEH discharging subcircuit is presented in Figure 11, illustrating very good correlation in voltage amplitude and similar deviations in discharging timestamps as observed in the charging process.

Custom commercial harvesting circuit (cc-ch). Measurements of the battery terminal voltage (V_B) and its charging current (I_B) at the cc-ch are shown in Figure 12 for excitation frequencies of 5, 10 and 15 Hz.

It is observed that as the excitation frequency is increased towards the eigenfrequency at 25 Hz, the frequency and the amplitude of the charging current pulses are increased as well. Thus, the harvesting power largely depends on the excitation frequency. However,

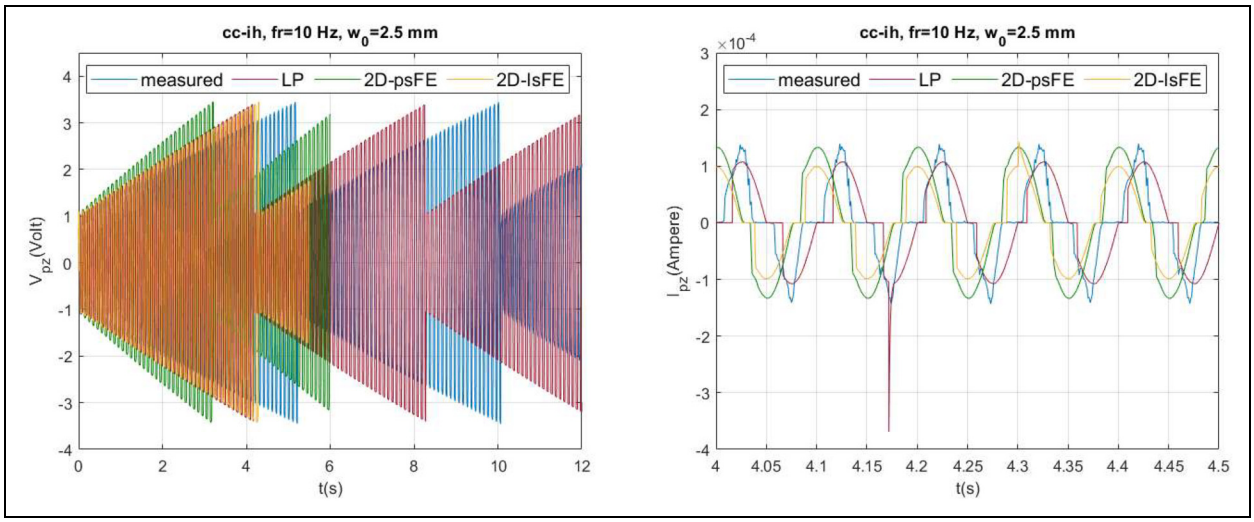

Figure 10. Measured and predicted response in capacitor of in-house harvesting circuit (cc-ih) at excitation frequency of 10 Hz.

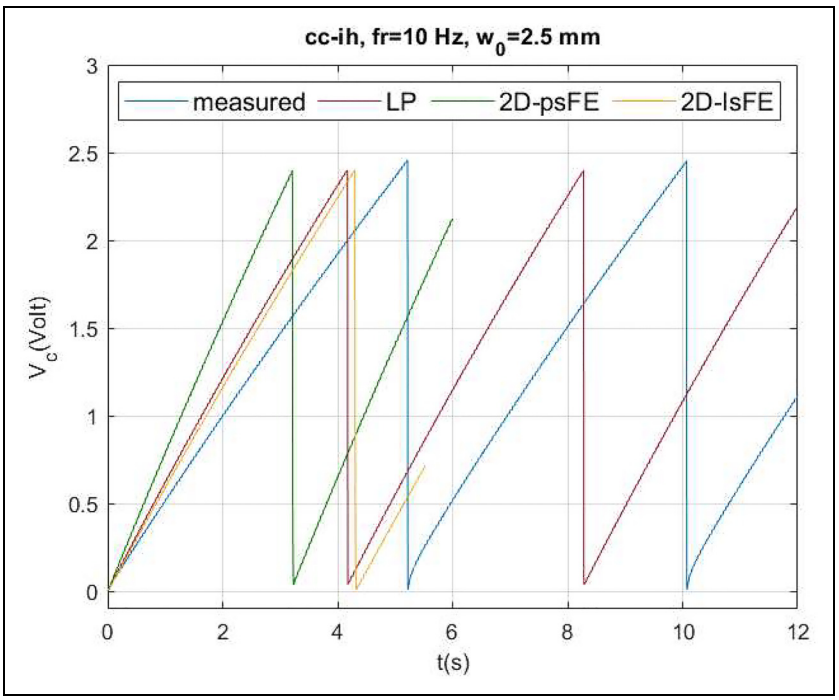

Figure 11. Measured and predicted output voltage of in-house harvesting circuit (cc-ih) at excitation frequency of 10 Hz.

the relationship is not proportional. Maximum harvesting power of 299.11 μW is observed in the experiment with excitation at 15 Hz, whereas 101.81 μW and 5 μW are obtained with excitation at 10 Hz and 5 Hz respectively.

Notably, the harvesting power at 5 Hz excitation is very small. A possible cause of this observation lies in the fact that the SPV1050 is not designed for oscillating inputs. Since the actual architecture and related parameters of the SPV1050 integrated circuit are not provided by the manufacturer, this assumption cannot be validated. However, it was necessary to increase the capacitance of the rectifier's output stage for the harvester to successfully switch on; the inserted capacitance acts as a low-pass filter. The maximum harvesting power of 5 μW has been reached using an electrolytic capacitor of 1000 μF.

Commercial harvesting circuit (cc-PI). Figure 13 shows the response of the voltage and the current at the input of cc-PI during the charging phase. The voltage is sinusoidal with increasing amplitude until it reaches 12 V, while the amplitude of the input current is decreasing. The comparison of measured and predicted response of the input signals during the charging phase shows that the LP model is successful in predicting the temporal evolution of the input voltage. However, the estimation of the input current is not as accurate, since it does not account for the energy consumed by the circuit for the operation of the automatic switch and the buck converter.

Figure 14 presents the input voltage and current of the harvesting circuit during the discharging phase. It is observed that during the discharging phase the input voltage continues to have a sinusoidal form with decreasing amplitude from 12 V to 6 V. The current slightly increases as the circuit's capacitor discharges.

Comparison of harvested power

The power harvested using each of the circuits is calculated using Equation (8). It was observed that variances in the initial charge of the charging capacitor may significantly alter the harvesting power. To this end, and for a fair comparison between the harvesting circuits, the timestamps considered should be selected within a time range of "settled" voltage and current signals, where the charge in the charging capacitor is stabilized to a steady-state range of values. In this context the experimentally determined harvested power for each circuit studied is listed in Table 3 for several frequencies. In Table 3 dashes denote zero output power.

Comparison of the values obtained indicates a general increase of output power with frequency. This is reasonable, as the fundamental eigenfrequency of the beam (24.9 Hz) is approached. Also, an approximate equivalence between modified commercial (cc-ch) and off-the -shelf commercial (cc-PI) circuits is observed at the low frequencies studied, whereas the in-house circuit (cc-ih) harvests power two orders of magnitude lower. This observation highlights the sensitivity of harvested power to circuit losses at the μW harvesting range, as the ones achieved experimentally. On the other hand, the in-house circuit is capable of harvesting at a wider frequency spectrum, including excitation frequencies as low as 1 Hz.

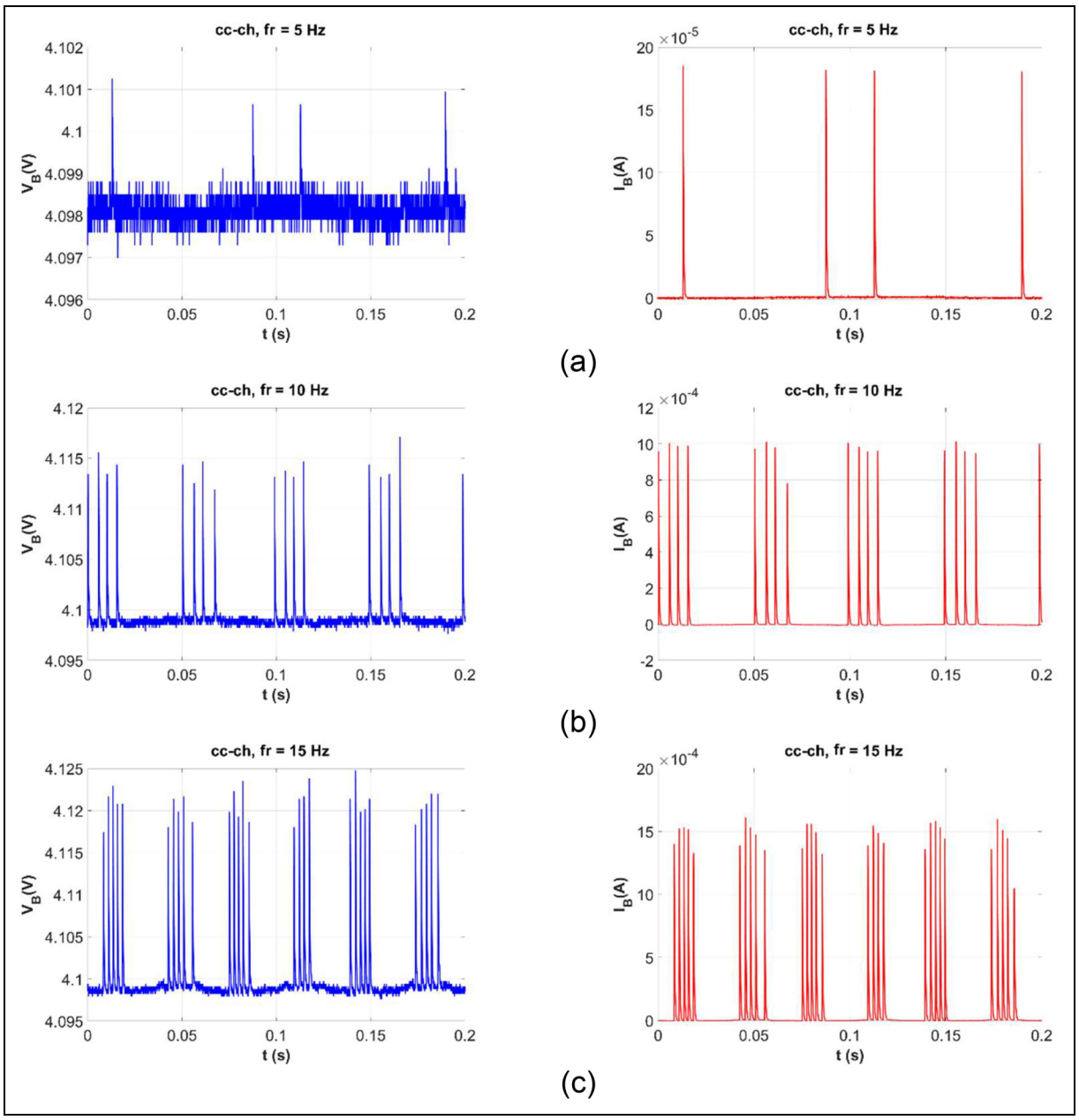

Figure 12. Measured battery's terminal voltage and charging current for the custom commercial harvesting circuit (cc-ch) at excitation frequencies of (a) 5 Hz, (b) 10 Hz, (c) 15 Hz.

Summary and conclusion

An experimental-numerical methodology has been developed for predicting the coupled electromechanical response of composite beams with harvesting circuits subjected to low, compared to resonance, frequency excitation. The modeling approach includes three FE models and a lumped parameter model, also FE-based. Validation with tests performed on an experimental configuration including a resistive and an in-house harvesting circuit illustrated the accuracy of each model. Further experiments using modified and off the shelf commercial harvesting circuits quantified their power harvesting capabilities. In the latter case reverse engineering led to a lumped parameter model capable of capturing the output voltage, whereas deviation was observed in prediction of output current.

The main conclusions drawn from the forced vibration response of the cantilever composite beam harvester with a PE transducer are listed below:

- The linear layerwise shell FE model (2D-lsFE) accurately captured the global closed-circuit response of the PEH in terms of output voltage and current, whereas predictions of the solid (3D-sFE) and plane strain (2D-psFE) models yielded deviations mainly attributed to composite material representation and thickness aspect ratio.

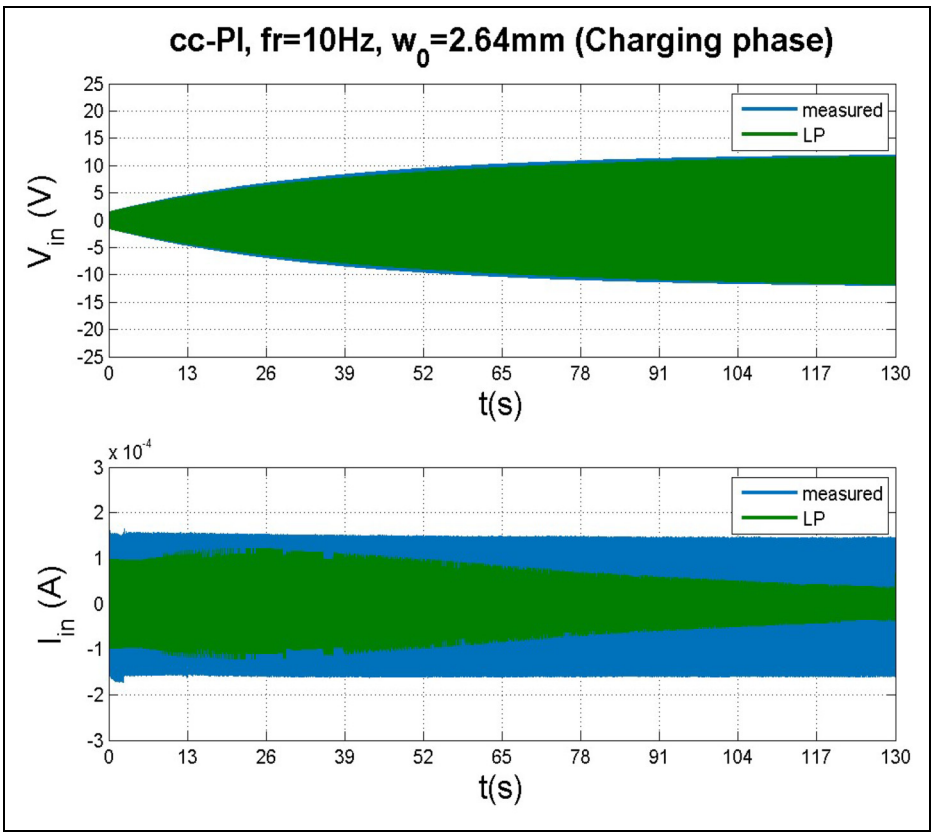

Figure 13. Measured and predicted response of input signals in the capacitor of the commercial harvesting circuit (cc-PI) at excitation frequency of 10 Hz.

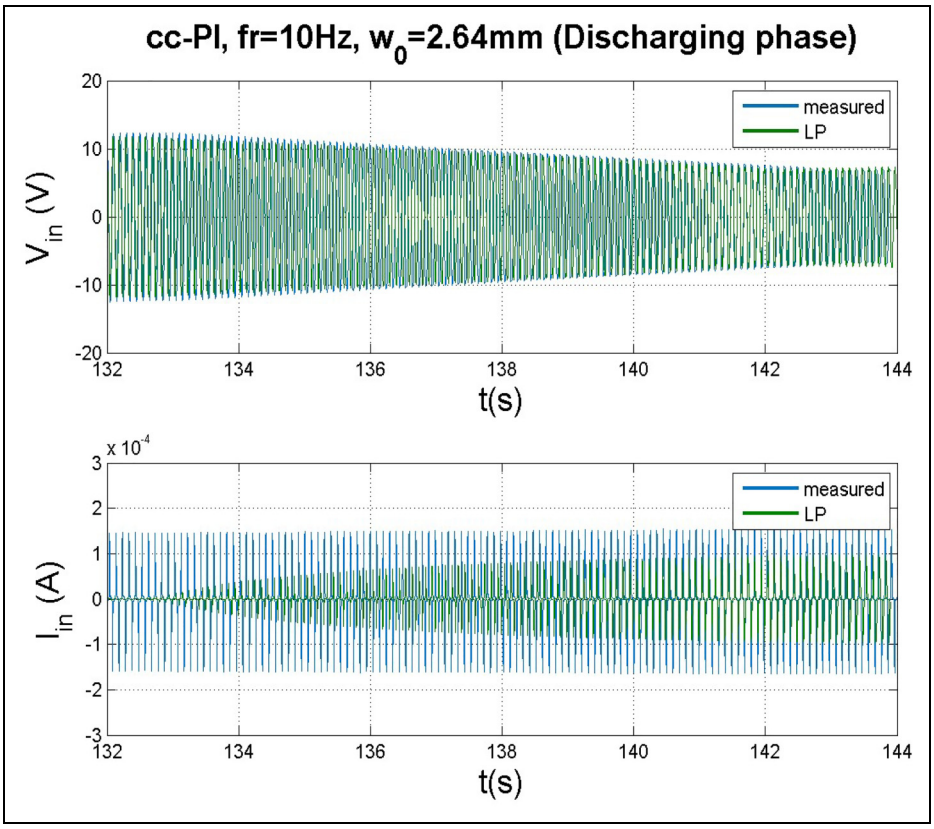

Figure 14. Measured and predicted response of input voltage and current signals in discharging branch of commercial harvesting circuit (cc-PI) at excitation frequency of 10 Hz.

Table 3. Harvested power by each of the PEH circuits considered.

Excitation Frequency [Hz]	P_{cc-ih} [μW]	P_{cc-PI} [μW]	P_{cc-ch} [μW]
1	1.0	–	–
5	1.1	–	5.4
10	1.3	89.8	101.8
15	1.7	256.4	299.1

- The plane strain FE model outperformed the other two FE models in terms of computational efficiency; hence, it is more suitable as a quick design tool.
- The lumped parameter modelling approach is the most efficient in terms of computational effort and approximates the layerwise shell FE model in accuracy of global response prediction.
- Small deviations were observed between predicted and measured voltage in the charging and discharging harvesting circuit branches, whereas electric current proved to be very sensitive to internal circuit losses in the μA range studied.
- Due to the linear regime of the mechanical response, and in all harvesting circuits studied, output power depends on frequency and increases as the eigenfrequency of the composite beam is approached.
- The commercial harvesting circuits provided equivalent power output in the low frequency excitation range beyond 5 Hz, whereas the in-house circuit yielded two orders of magnitude less power. However, the latter is also capable of power output below 5 Hz, which may be a useful feature in specific applications.

The numerical-experimental methodology studied the performance of a composite PEH beam in the low-frequency range and provided valuable insight regarding modeling of the electromechanical response in closed-circuit configurations.

Acknowledgements

This research has been co-financed by the European Regional Development Fund of the European Union and Greek national funds through the Operational Program Competitiveness, Entrepreneurship, and Innovation, under the call RESEARCH – CREATE – INNOVATE (project code: T1EDK-01533). The contribution of the Structural Mechanics and Smart Materials Group of the University of Patras in damping characterization of the composite beam and selection of equipment is gratefully acknowledged.

Declaration of Conflicting Interests

The author(s) declared no potential conflicts of interest with respect to the research, authorship, and/or publication of this article.

Funding

The author(s) disclosed receipt of the following financial support for the research, authorship, and/or publication of this article: This work was supported by the European Union and Greek National Funds (grant number T1EDK-01533). This research has been co-financed by the European Regional Development Fund of the European Union and Greek national funds through the Operational Program Competitiveness, Entrepreneurship, and Innovation, under the call RESEARCH– CREATE – INNOVATE (project code: T1EDK-01533).

ORCID iD

Theofanis S. Plagianakos https://orcid.org/0000-0002-3577-7333

Supplemental material

Supplemental material for this article is available online.

References

1. Kymissis J, Kendall C and Paradiso J, et al. Parasitic power harvesting in shoes. In: *Second international symposium on wearable computers*, Pittsburgh, US, 19–20 October 1998. DOI: 10.1109/ISWC.1998.729539.
2. Elvin NG, Elvin AA and Spector M. A self-powered mechanical strain energy sensor. *Smart Mater Struct* 2001; 10: 293–299 DOI: 10.1088/0964-1726/10/2/314.
3. Erturk A and Inman DJ. *Piezoelectric energy harvesting*. UK: John Wiley and Sons Ltd, 2011.
4. Cook-Chennault KA, Thambi N and Sastry AM. Powering MEMS portable devices – a review of non-regenerative and regenerative power supply systems with special emphasis on piezoelectric energy harvesting systems. *Smart Mater Struct* 2008; 17: 043001 DOI: 10.1088/0964-1726/17/4/043001.
5. Mitcheson PD, Yeatman EM and Kondala Rao G, et al. Energy harvesting from human and machine motion for wireless electronic devices. *Proc IEEE* 2008; 96: 1457–1486.
6. Safaei M, Sodano HA and Anton SR. A review on energy harvesting using piezoelectric materials: state-of-the-art a decade later (2008-2018). *Smart Mater Struct* 2019; 28: 1–63.
7. Guyomar D and Lallart M. Recent progress in piezoelectric conversion and energy harvesting using nonlinear electronic interfaces and issues in small scale implementation. *Micromachines-Basel* 2011; 2: 274–294.
8. Ottman GK, Hoffmann HF and Bhatt AC, et al. Adaptive piezoelectric energy harvesting circuit for wireless remote power supply. *IEEE T Power Electr* 2002; 17: 669–676.
9. Tabesh A and Frechette LG. A low-power stand-alone adaptive circuit for harvesting energy from a piezoelectric micropower generator. *IEEE T Ind Electron* 2010; 57: 840–849.
10. Guyomar D, Badel A and Lefeuvre E, et al. Toward energy harvesting using active materials and conversion improvement by non- linear processing. *IEEE T Ultrason Ferr* 2005; 52: 584–595.
11. Wu L, Do XD and Lee SG, et al. A self-powered and optimal SSHI circuit integrated with an active rectifier for piezoelectric energy harvesting. *IEEE T Circuits-I* 2017; 64: 537–549.
12. Kawai N, Kushino Y and Koizumi H. MPPT controlled piezoelectric energy harvesting circuit using synchronized switch harvesting on inductor. In: *Proceedings of the IECON2015*, Yokohama, Japan, 9–12 November 2015. DOI: 10.1109/IECON.2015.7392250.

13. Ramadass YK and Chandrakasan AP. An efficient piezoelectric energy harvesting interface circuit using a bias-flip rectifier and shared inductor. *IEEE J Solid-St Circuits* 2010; 45: 189–204.
14. Jia Y. Review of nonlinear vibration energy harvesting: duffing, bistability, parametric, stochastic and others. *J Intel Mat Sys Str* 2020; 31: 921–944.
15. Huguet T, Lallart M and Badel M. Bistable vibration energy harvester and SECE circuit: exploring their mutual influence. *Nonlinear Dynam* 2019; 97: 485–501.
16. Wang J, Zhao B and Liao WH, et al. New insight into piezoelectric energy harvesting with mechanical and electrical nonlinearities. *Smart Mater Struct* 2020; 29: 04LT01.
17. Roundy S, Wright PK and Rabaey JM. A study of low level vibrations as a power source for wireless sensor nodes. *Comput Commun* 2003; 26: 1131–1144.
18. Erturk A and Inman DJ. A distributed parameter electromechanical model for cantilevered piezoelectric energy harvesters. *J Vib Acoust* 2008; 130: 041002.
19. Goldfarb M and Celanovic N. A lumped parameter electromechanical model for describing the nonlinear behavior of piezoelectric actuators. *J Dyn Sys, Meas, Control* 1997; 119: 478–485.
20. Touairi S and Mabrouki M. Control and modelling evaluation of a piezoelectric harvester system. *Int J Dyn Control* 2021. in press. DOI: 10.1007/s40435-021-00764-w
21. Onsorynezhad S, Abedini A and Wang F. Parametric optimization of a frequency-up-conversion piezoelectric harvester via discontinuous analysis. *J Vib Control* 2020; 26: 1241–1252.
22. Liao Y and Liang J. Unified modeling, analysis and comparison of piezoelectric vibration energy harvesters. *Mech Syst Signal Pr* 2019; 123: 403–425.
23. Harne RL and Wang KW. A review of the recent research on vibration energy harvesting via bistable systems. *Smart Mater Struct* 2013; 22: 023001 DOI: 10.1088/0964-1726/22/2/023001.
24. Jacquelin E, Adhikari S and Friswell MI. A piezoelectric device for impact energy harvesting. *Smart Mater Struct* 2011; 20: 105008 DOI: 10.1088/0964- 1726/20/10/105008.
25. Benasciutti D, Moro L and Gallina M. On the optimal bending deflection of piezoelectric scavengers. *J Intel Mat Sys Str* 2012; 24: 627–639 DOI: 10.1177/1045389X12469451.
26. Wang H, Shan X and Xie T. Performance optimization for cantilevered piezoelectric energy harvester with a resistive circuit. In: *Proceedings of the IEEE ICMA*, Chengdu, China, 5–8 August 2012. DOI: 10.1109/ICMA.2012.6285680.
27. Rezaeisaray M, El Govini M and Sameoto D, et al. Low frequency piezoelectric energy harvesting at multi vibration mode shapes. *Sensor Actuat A-Phys* 2015; 228: 104–111 DOI: 10.1016/j.sna.2015.02.036.
28. Niasar EHA, Dahmardeh M and Googarchin HS. Roadway piezoelectric energy harvester design considering electrical and mechanical performances. *Proc. JMech E Part C: J Mech Eng Sci* 2020; 234: 32–48 DOI: 10.1177/0954406219873366.
29. Niasar EHA, Dahmardeh M and Googarchin HS. Optimization of a piezoelectric energy harvester considering electrical fatigue. *J Intel Mat Sys Str* 2020; 31: 1443–1454 DOI: 10.1177/1045389X20923086.
30. Chen K, Gao F and Liu Z, et al. A nonlinear M-shaped tridirectional piezoelectric energy harvester. *Smart Mater Struct* 2021; 30: 045017 DOI: 10.1088/1361- 665X/abe87e.
31. Kardarakos GC, Chrysochoidis NA and Varelis D, et al. Computational and experimental efficiency investigation of nonlinear energy harvesting systems based on monostable and bistable piezoelectric beams. SMASIS 2021, paper no. 68209, in press.
32. Comsol AB. *Comsol Multiphysics Reference Manual*, v. 5.6, 2020.
33. Saravanos DA, Heyliger PR and Hopkins DA. Layerwise mechanics and finite element for the dynamic analysis of piezoelectric composite plates. *Int J Solids Struct* 1997; 34: 359–378.
34. Barbero EJ. *Finite element analysis of composite materials using Abaqus*. Boca Raton FL-US: CRC Press, 2013.
35. Plagianakos TS and Saravanos DA. Hybrid multidamped composite plates with viscoelastic composite plies and shunted piezoelectric layers. *J Intel Mat Sys Str* 2003; 14: 57–66.
36. Walgrave SC and Ehlbec JM. Understanding modal analysis. *Soc Automobile Eng Trans* 1978; 87: 2695–2705.
37. Plagianakos TS and Papadopoulos EG. Higher-order 2-D/3-D layerwise mechanics and finite elements for composite and sandwich composite plates with piezoelectric layers. *Aerosp Sci Technol* 2015; 40: 150–163.
38. Mathworks. *Simscape TM User's Guide (2020a)*, 2020.
39. PSpice® User Guide – Product Version 17.2-2016. *Cadence Design Systems, Inc*.
40. SPV1050. Ultra low power energy harvester and battery charger with embedded MPPT and LDOs. https://www.stcom/en/power-management/spv1050.
41. E-821 Electronic module for energy harvesting using piezo actuators for energy generation. *PI Motion/Positioning*, 2014.
42. https://www.piceramic.com/en/ (accessed 10 October 2020).
43. Komitopoulos S. *Active vibration control of composite beams using piezoelectric transducers and real-time software*. MS Thesis, National Technical University of Athens, GR, in progress.
44. Plagianakos TS, Muñoz K and Gouillamet G, et al. Assessment of CNT-doping and hot-wet storage aging effects on mode I, II and I/II interlaminar fracture toughness of a UD graphite/epoxy material system. *Eng Fract Mech* 2020; 224: DOI: 10.1016/j.engfracmech.2019.106761.

List of Abbreviations

3D-sFE	Three-Dimensional solid Finite element
2D-psFE	Two-Dimensional plane strain Finite Element
2D-lsFE	Two-Dimensional layerwise shell Finite Element
AC	Alternating Current
cc	closed-circuit
cc-ih	closed-circuit in-house harvester
cc-ch	closed-circuit modified commercial harvester
cc-PI	closed-circuit Physik Instrumente
cc-R	closed-circuit Resistive
DAQ	Data Acquisition

DOF	Degrees of Freedom
DC	Direct Current
FE	Finite Element
IC	Integrated Circuit
IoT	Internet of Things
LiPo	Lithium Polymer
LP	Lumped Parameter
MOSFET	Metal-Oxide Semiconductor Field-Efficient Transistor
MPPT	Maximum Power Point Tracking
oc	open-circuit
PE	Piezoelectric
PEH	Piezoelectric Energy Harvesting
SSHI	Synchronized Switch Harvesting on Inductor